

Research Paper

Identification of type IV collagen exposure as a molecular imaging target for early detection of thoracic aortic dissection

Ke Xu^{1*}, Chen Xu^{2*}, Yanzhenzi Zhang¹, Feiran Qi¹, Bingran Yu², Ping Li¹, Lixin Jia¹, Yulin Li¹✉, Fu-jian Xu²✉, Jie Du¹✉

1. Beijing Anzhen Hospital, Capital Medical University; Key Laboratory of Remodeling-Related Cardiovascular Diseases, Ministry of Education; Beijing collaborative innovative research center for cardiovascular diseases; Beijing Institute of Heart Lung and Blood Vessel Diseases, Beijing 100029 China;
2. Beijing Laboratory of Biomedical Materials, Key Laboratory of Carbon Fiber and Functional Polymers (Beijing University of Chemical Technology), Ministry of Education, Beijing University of Chemical Technology, Beijing 100029 China.

* These authors contributed equally to this work.

✉ Corresponding authors: Email: jiedu@ccmu.edu.cn (J.D.); xufj@mail.buct.edu.cn (Fj.X.); lyllyl_1111@163.com (Yl. L.)

© Ivyspring International Publisher. This is an open access article distributed under the terms of the Creative Commons Attribution (CC BY-NC) license (<https://creativecommons.org/licenses/by-nc/4.0/>). See <http://ivyspring.com/terms> for full terms and conditions.

Received: 2017.08.21; Accepted: 2017.10.22; Published: 2018.01.01

Abstract

Thoracic aortic dissection (TAD) is an aggressive and life-threatening vascular disease and there is no effective means of early diagnosis of dissection. Type IV collagen (Col-IV) is a major component of the sub-endothelial basement membrane, which is initially exposed followed by endothelial injury as early-stage event of TAD. So, we want to build a noninvasive diagnostic method to detect early dissection by identifying the exposed Col-IV via MRI.

Methods: Col-IV-targeted magnetic resonance/ fluorescence dual probe (Col-IV-DOTA-Gd-rhodamine B; CDR) was synthesized by amide reaction and coordination reaction. Flow cytometry analysis was used to evaluate the cell viability of SMC treated with CDR and fluorescence assays were used to assess the Col-IV targeting ability of CDR *in vitro*. We then examined the sensitivity and specificity of CDR at different stages of TAD via MRI and bioluminescence imaging *in vivo*.

Results: The localization of Col-IV (under the intima) was observed by histology images. CDR bound specifically to Col-IV-expressing vascular smooth muscle cells and BAPN-induced dissected aorta. The CDR signal was co-detected by magnetic resonance imaging (MRI) and bioluminescence imaging as early as 2 weeks after BAPN administration (pre-dissection stage). The ability to detect rupture of dissected aorta was indicated by a strong normalized signal enhancement (NSE) *in vivo*. Moreover, NSE was negatively correlated with the time of dissection rupture after BAPN administration ($r^2 = 0.8482$).

Conclusion: As confirmed by *in vivo* studies, the CDR can identify the exposed Col-IV in degenerated aorta to monitor the progress of aortic dissection from the early stage to the rupture via MRI. Thus, CDR-enhanced MRI proposes a potential method for dissection screening, and for monitoring disease progression and therapeutic response.

Key words: Thoracic aortic dissection, Early diagnosis, Risk prediction, Magnetic resonance imaging, Fluorescence imaging.

Introduction

Thoracic aortic dissection (TAD) is an aggressive and life-threatening vascular disease [1, 2]. Epidemiological studies suggest an incidence of acute aortic dissection of about 7–9 cases per 100 000 people per year [3]. The incidence of TAD has increased by

5% per year in recent years, due to increased prevalence of hypertension [4]. TAD is defined as disruption of the medial layer, and is caused by intramural bleeding leading to separation of the aortic wall layers followed by formation of a true lumen and

a false lumen. In most cases, the dissection develops without aneurysmal degeneration and clinical manifestation [5], so the TAD cannot be detected in a regular physical examination. Dissection will expand rapidly leading to serious complications, such as rupture or organ ischemia. The mortality of acute TAD is 1%–2% per hour during the first day, while almost half of all patients die by 1 week, and the 1-year mortality is 90% [6]. Currently, there is no treatment to reverse this disease.

The clinical diagnosis of TAD relies on imaging tests, including computed tomography angiography (CTA), magnetic resonance imaging (MRI), and transthoracic echocardiography (TTE). Guidelines recommend TTE, CTA, or both for preliminary screening of patients with suspected acute aortic dissection in an emergency room, and MRI is commonly used to evaluate the aorta before and after treatment [7-9]. These methods can diagnosis the dissection (including true/false lumen, location and extent of dissection), but they cannot provide early detection of dissection before intimal tear. Thus development of molecular imaging, which combines the early characteristic pathological processes and classic imaging, is needed for early detection of TAD.

Application of in-depth knowledge of the pathological process into classic imaging has now entered the era of molecular imaging, with molecular probes designed to target specific molecules in pathological tissues. For example, A β oligomerization is an early event in Alzheimer's disease [10]; thus, use of oligomer-specific antibodies conjugated to magnetic nanostructures to bind A β oligomers allows for early detection of Alzheimer's disease by MRI [11]. Furthermore, increased fibronectin expression (a hallmark of epithelial-mesenchymal transition) is a signal for early metastasis of breast cancer [12], and a fibronectin-targeting contrast agent could detect breast cancer micro-metastasis using MRI [13].

Studies have shown that intimal tearing caused by long-term chronic stimulation is preceded by medial degeneration or cystic medial necrosis during TAD development [14-16]. Progressive endothelial injury occurs before intimal tearing, including endothelial cell (EC) loss, increased permeability, and subsequent exposure of the sub-endothelial basement membrane [17, 18]. Type IV collagen (Col-IV) is a major component of the sub-endothelial basement membrane, which is initially exposed at sites of EC loss [19]. Farokhzad et al. first showed that Col-IV is a major component of the vascular basement membrane that becomes exposed at sites of vessel injury [20]. This group designed a Col-IV-targeted nanoparticle containing an anti-inflammatory peptide (Ac2-26), which effectively targeted atherosclerotic lesions and

promoted inflammation resolution [21]. Similarly, a Col-IV-targeting peptide was employed to improve targeting to the atherosclerotic plaque [22].

Here, we tested the hypothesis that molecular MRI targeting of exposed Col-IV at sites of endothelial injury may provide early detection of TAD. Specifically, we constructed a type IV collagen-targeted MRI probe, Col-IV-DOTA-Gd-RhB, and demonstrated its ability to detect early dissection in a mouse model of TAD, as well as show its capacity to predict rupture of the dissection.

Materials

Human aorta samples

We collected six thoracic aorta wall samples from patients with TAD (Stanford type A and type B) and five internal mammary arteries (bridge vessel pruning) from myocardial infarction patients (without intima injury, atherosclerotic plaque or diameter dilation) during coronary artery bypass surgery at Anzhen Hospital cardiac surgery center (Beijing, China) between September 2015 and April 2016. This study was approved by the Ethics Review Board of Beijing Anzhen Hospital.

Ethics statement

All animal care and experimental protocols complied with the Animal Management Rule of the Ministry of Health, People's Republic of China (Documentation no. 55, 2001) and the Guide for the Care and Use of Laboratory Animals published by the US National Institutes of Health (NIH Publication no. 85-23, revised 1996). All procedures were approved by the Institutional Animal Care and Use Committee of Capital Medical University, Beijing, China.

Animals and TAD experimental models

C57BL/6J male mice were purchased from Beijing HFK Bioscience Co. Ltd. (Beijing, China.). Three-week-old male mice were fed a regular diet and administered 3-aminopropionitrile fumarate salt (BAPN) (Sigma-Aldrich, St. Louis, MO, USA) dissolved in drinking water (1 g/kg/day) for 4 weeks, as described previously [23]. For aortic tissue analysis, mice were sacrificed after 2, 3, and 4 weeks of BAPN administration. These time points were chosen based on our previous observations with this model [24]. At the end of the experiment, mice were euthanized by overexposure to isoflurane, and the entire thoracic aorta was dissected and fixed in 4% paraformaldehyde for further pathological analyses.

Materials

The following reagents were used: rhodamine B (RhB)-Cys-Gly-Gly-Gly-Lys-Pro-Leu-Val-Trp-Leu-Ly

s (CGGGKPLVWLK; Col-IV-RhB, 97.92%, SciLight Biotechnology Ltd. Co., Beijing, China), gadolinium trichloride hexahydrate ($\text{GdCl}_3 \cdot 6\text{H}_2\text{O}$, 99.99%, Energy Chemical, Shanghai, China), 1,4,7,10-tetraazacyclododecane-1,4,7,10-tetraacetic acid 1-(2,5-dioxo-1-pyrrolidinyl) ester (DOTA-NHS ester, CheMatech, Dijon, France), sodium bicarbonate (NaHCO_3 , 99.5%) [25].

Synthesis of Col-IV-DOTA-RhB (CDR)

To generate the functional material, DOTA-NHS ester was first complexed with gadolinium. DOTA-NHS ester (12.66 mg, 0.025 mmol) and NaHCO_3 (6.40 mg, 0.076 mmol) were dissolved in 1 mL deionized water for salinization. The reaction mixture was stirred at room temperature for 10 min, and $\text{GdCl}_3 \cdot 6\text{H}_2\text{O}$ (9.39 mg, 0.025 mmol) was then added into the system and complexing was carried out for ~4 h at room temperature. Finally, Col-IV-RhB (20.00 mg, 0.013 mmol) dissolved in 2 mL of deionized water was dripped slowly into the system. The resultant mixture was stirred at 4 °C for 12 h and the final products were lyophilized.

Characterization of CDR

The synthesized material was tested by high performance liquid chromatography (HPLC) on a C18 LC-20AT HPLC column with methanol: water: trifluoroacetic acid (9:1:0.005) as the eluent at a low-flow rate of 1.0 mL/min and temperature of 27 °C, and detected at 254 nm. All the solvents were chromatography grade and both samples were dissolved in water at a concentration of 1 mg/mL. The ultraviolet absorbance and fluorescence intensity of CDR were measured using an ultraviolet spectrophotometer (UV-2600, Shimadzu) and a fluorescence photometer (F-7000, Hitachi), respectively. The ultraviolet / visible light absorbance signal of CDR was detected from 450 nm to 650 nm by excitation with ultraviolet light, after correcting for baseline values. After adjustments, we selected 535 nm as the optimal excitation wavelength for determining the fluorescence intensity of CDR, and 550 nm as the beginning of the emission band for different concentration of CDRs (0.01 mg/mL to 0.1 mg/mL, a total of 10 groups).

Cell culture

Three cell lines were passaged when they reached ~80% confluence following digestion with 0.25% trypsin. Smooth muscle cells (SMCs) were cultured in DMEM medium (HyClone, Waltham, MA, USA) supplemented with 10% heat-inactivated fetal bovine serum (FBS) (Gibco, USA) and 1% penicillin/streptomycin (Gibco). Human umbilical vein vascular endothelial cells were cultured in Endothelial Basal Medium (EBM-2; Lonza,

Switzerland) containing 20% FBS and 1% penicillin/streptomycin. Macrophages (bone marrow derived macrophage, BMM) were cultured in DMEM medium supplemented with 10% FBS in the presence of 50 ng/mL macrophage colony-stimulating factor and 1% penicillin/streptomycin [26].

CDR toxicity test

In vitro cytotoxicity was detected by flow cytometry analysis. Cell cultures were prepared by standard procedures, and incubated with CDR for 24 h in different Gd^{3+} concentrations (0, 0.2, 0.5, 0.7, 1.0, 5.0 μM) with serum-free medium. Cell suspensions were then prepared by digestion with 0.25% trypsin. The cells were then stained with Hoechst dye for 15 min and analyzed using a Beckman Coulter Epics XL flow cytometer (Beckman Coulter, Miami, FL, USA) as described previously [27].

In vitro detection of CDR-targeting and fluorescence abilities

In vitro fluorescence assays were performed in SMCs, ECs, and macrophages. Briefly, the cells were incubated with CDRs at different Gd^{3+} concentrations (0, 0.2, 0.5, 0.7, 1.0, 5.0 μM). After 4 h, the cells were washed with phosphate-buffered saline (PBS), and cultured in fresh serum-free medium for another 20 h. The SMCs were washed with PBS and stained with DAPI, and the average fluorescence intensity was then measured to assess the fluorescence ability of CDR using ImageXpress Micro system (Molecular Devices, USA). In addition, the RhB-positive cell ratio was measured to assess the ability of CDR to target Col-IV.

Immunohistochemistry and immunofluorescence

For animal studies, the descending aorta was excised, embedded in optimal cutting temperature compound, sectioned, and stained for immunohistochemistry and immunofluorescence using the following primary antibodies: rabbit anti-mouse Col-I, rabbit anti-mouse Col-III collagen, rabbit anti-mouse Col-IV, mouse anti-mouse α -smooth muscle actin, and rat anti-mouse CD31 (Abcam Inc., Cambridge, MA, USA). For cell studies, SMCs, ECs, and macrophages were plated on Lab-Tek chamber slides, washed three times with PBS, fixed in 4% paraformaldehyde for 10 min, and then permeabilized for 10 min with 0.2% Triton X-100 at room temperature. The cells were then immunostained using a primary rabbit anti-mouse Col-IV antibody.

Elastin staining

Elastin in control and TAD mouse aortas was

stained using Gomori's aldehyde-fuchsin staining method, with elastic-fiber stain kit (Maixin Bio, Fuzhou, China). In brief, sections were incubated for 5 min in Lugol's iodine solution, washed twice with PBS, and then incubated with sodium thiosulfate for 5 min. Sections were then washed with running tap water for 5 min followed by 70% ethanol, incubated with aldehyde-fuchsin for 10 min, washed with 70% ethanol until they no longer bleached, and stained with acid orange G for 10 s.

Sirius Red staining

Collagen was stained directly using Sirius Red (Direct Red 80; Sigma-Aldrich, Cat#365548 or 43665) and saturated aqueous picric acid (1.3% in water; Sigma; Cat# P6744-1GA). In brief, nuclei were stained with Weigert's hematoxylin for 8 min, and then washed for 10 min in running tap water, followed by staining with picric-Sirius Red for 1 h, and then washed in two changes of acidified water. This achieved near-equilibrium staining that did not increase with longer staining times, while shorter times were not sufficient, even when the colors appeared adequate. Slides were then dehydrated in three changes of 100% ethanol, cleared in xylene, and mounted in a resinous medium. The results were observed using a polarized microscope.

Transthoracic echocardiography

Transthoracic ultrasound of TAD model mice was performed using a Vevo 2100 imaging system (VisualSonics, Toronto, Canada) equipped with an integrated isoflurane-based anesthesia system as described [28]. Mice were examined after 0, 1, 2, 3, and 4 weeks of BAPN administration. Short-axis scans of the ascending or descending aorta were performed. The maximum diameter of the thoracic aorta was measured by M-mode. After the end of the experiment, the mice were euthanized with excess isoflurane and the thoracic aorta was collected for follow-up experiments.

Endothelial injury assay

Aorta endothelial injury was assessed by staining with Evans Blue dye (Sigma), as described previously [30]. Briefly, 100 μ L 5% Evans blue diluted in saline was injected into the angular vein. After 20 min, mice were euthanized by overexposure to isoflurane, and the thoracic aorta was washed with saline (to wash off the Evans blue dye remaining in the aorta) and fixed with 4% paraformaldehyde for 10 min. Then the thoracic aorta was removed, cut along the long axis of the vessels to expose the intima, and tiled on a glass slide (the adventitia surface was contacted with the slide). The blue-stained injured endothelium was observed by stereoscopic

microscopy (SMZ745T, Nikon, Japan).

Bioluminescence imaging

Fluorescence imaging was performed using an *in vivo* imaging system (Leica) using the appropriate filters for RhB (excitation: 535 nm; emission: 550 nm long-pass filter). Mice exposed to BAPN for 0, 2, or 4 weeks were injected with CDR (10 nmol RhB per mouse) and RhB fluorescence images of TAD aortae were acquired. The fluorescence signal was analyzed with region-of-interest (ROI)-measuring software to subtract background autofluorescence.

Relaxivity of CDR

MRI experiments were performed using a 7.0 T MRI instrument (Biospec 70/20USR7.0T Bruker). To investigate the performance of this new contrast agent, the relaxivities of unbound and bound CDR were determined using a 7.0 T MRI instrument (Biospec 70/20 USR 7.0T Bruker). Unbound CDR solutions at different concentrations (Gd^{3+} = 0, 5, 10, 15, 20, 25, 30 M) were scanned by MRI to determine the relaxivity at 7 T. CDR solutions in 0.2 mL tubes were placed in a rat head/mouse body coil (Agilent Technologies) using a T1 mapping RARE sequence (repetition time = 400, 800, 1500, 2500, 4000 ms; echo time = 7 ms; field of view: 4.0 cm², matrix: 256 \times 256; number of excitations: 2.0; slice thickness = 1 mm; slice gap = 0). The R1 value was measured using Matlab software. For the bound study, SMCs were incubated with increasing amounts of CDR (0–30 μ M) at 37 °C for 24 h, washed three times with PBS, precipitated by centrifugation at 362 \times g for 10 min, rinsed three times with PBS, trypsin digested, and then transferred to 0.2 mL tubes. T1 relaxivity was measured as for the unbound CDR.

In vivo MRI

In vivo MRI examinations were performed using a Bruker Biospec 7T MRI scanner (Biospec 70/20 USR 7.0T Bruker) with a mouse head/mouse body coil. Mice were anesthetized with a 2% isoflurane-oxygen mixture in an isoflurane induction chamber. A respiratory sensor connected to a monitoring system (SA Instruments, Stony Brook, NY, USA) was placed on the abdomen to monitor the respiration rate and depth. Images were acquired using a T1-weighted black blood sequence with respiratory gating and electrocardiogram-triggered gating before injection (Sequence 1: repetition time 1/4 923.06 ms, echo time 1/4 2.74 ms, inversion time T1: 773.06 ms, number of excitations: 2.0, average 1/4 3, flip angle: 30°, field of view: 3.0 cm², matrix: 256 \times 256, scan duration with respiratory gating: 20 min). After pre-injection baseline MR imaging, commercial DOTA-Gd (CG) or CDR was injected via the angular vein at a dose of

2.66 mg of Gd per mouse by flushing with 100 μ L saline, and the T1-weighted black blood sequence was acquired after 20 min.

Image analysis

MR images were analyzed using OsiriX DICOM Viewer (Geneva, Switzerland), using the spinal cord as a landmark. After CDR injection, ROIs were drawn around the enhancement area within the TAD wall. Average signal intensity in these ROIs ($SI_{\text{enhanced area}}$) was measured over three slices throughout the dissection. Additional ROIs were also drawn in the surrounding muscle, as well as in the noise, to determine the mean deviation of the noise (I_{muscle} , σ_{noise} , respectively). Signal to noise ratio (SNR), contrast to noise ratio (CNR), and the normalized percentage signal enhancement (%NSE) were calculated for the wall and muscle according to the following equations. The data are presented as mean \pm standard deviation (SD).

$$\text{SNR} = SI_{\text{enhanced area}} / SD_{\text{noise}}$$

$$\text{CNR}_{\text{WM}} = \text{SNR}_{\text{wall}} / \text{SNR}_{\text{muscle}}$$

$$\text{CNR}_{\text{norm}} = \text{CNR}_{\text{WMpost}} / \text{CNR}_{\text{WMpre}}$$

$$\% \text{NSE} = [(\text{CNR}_{\text{WM}} - \text{CNR}_{\text{norm}}) / \text{CNR}_{\text{norm}}] \times 100.$$

Statistical analysis

Statistical analysis was performed using SPSS 23.0 (SPSS Inc., Chicago, IL, USA). Graphs were drawn using GraphPad Prism 6 (GraphPad Software, San Diego, CA, USA). Normality analysis was performed before any testing via the Kolmogorov-Smirnov test. The differences between two groups were analyzed by unpaired Student's *t*-tests, and One-way ANOVA was conducted followed by Bonferroni post hoc test for comparisons between >2 groups. The non-normal distributed data were analyzed using non-parametric testing (Mann-Whitney U test for two groups and Krushal-Wallis H test for >2 groups). If the measurement data followed a normal distribution, the data are expressed as mean values \pm standard deviation (SD); if not, the data are expressed as median values \pm interquartile range (IQR). We ran a normality test (Kolmogorov-Smirnov test) for measurement data. For the normal distribution of data, we used the Pearson's correlation test; for the skewed distribution of data, we use the Spearman's correlation test. P values less than 0.05 were considered statistically significant.

Results

Loss of endothelial cells at early stage of TAD development

3-week-old C57BL/6 mice were administered with BAPN for 4 weeks to replicate the clinical process of TAD. Elastin staining revealed slight disordering of elastic fibers that could be detected in the aortic arch after 2 weeks of BAPN administration; disruption of elastic fiber cross-linking and slight dissection appeared after 3 weeks, and typical TAD after 4 weeks (Fig. 1A). The results of gross examination and ultrasonography were consistent with the elastin staining (Fig. 1B, C). However, EC loss, indicated by Evans blue staining, occurred as early as the first week of BAPN administration, and the area of EC loss increased with progressive development of TAD (Fig. 1D). Analysis of vascular dilation and dissection rupture rates at different time points indicated that the rupture rate was nearly 15% after 2 weeks of BAPN administration and vascular dilation was significant after 3 weeks of BAPN administration (Fig. 1E, F). These results suggested that EC loss preceded vascular dilation and elastic-fiber degradation during the development of TAD.

Exposure of Col-IV was an early event of TAD development

Col-IV is a basement membrane-specific collagen localized beneath the ECs [19]. We determined the locations and expression of Col-I, Col-III, and Col-IV during the development of TAD. Immunofluorescence staining showed Col-I and Col-III were predominantly expressed in adventitia, while only Col-IV was expressed under the intima of normal vasculature (Fig. 2A). Sirius Red staining showed the localization of three kinds of collagen at different stages of TAD: Col-IV was localized under intima, while Col-I and Col-III were located in adventitia (Fig. 2B). Immunofluorescence staining of Col-IV at different stages of TAD also confirmed its specific localization, and the Col-IV content gradually increased with BAPN administration (Fig. 2C). The Col-IV-positive area (%) increased linearly with increasing weeks of BAPN administration ($r^2 = 0.96$, $p < 0.0001$) (Fig. 2D). We next examined the location of Col-IV in thoracic aorta tissues from normal humans and TAD patients, and found that Col-IV was also located under the intima, and the Col-IV-positive area (%) in the vasculature was significantly higher in TAD patients compared with normal controls (Fig. 2E, F). These results demonstrated that exposure of Col-IV is an early event in TAD development.

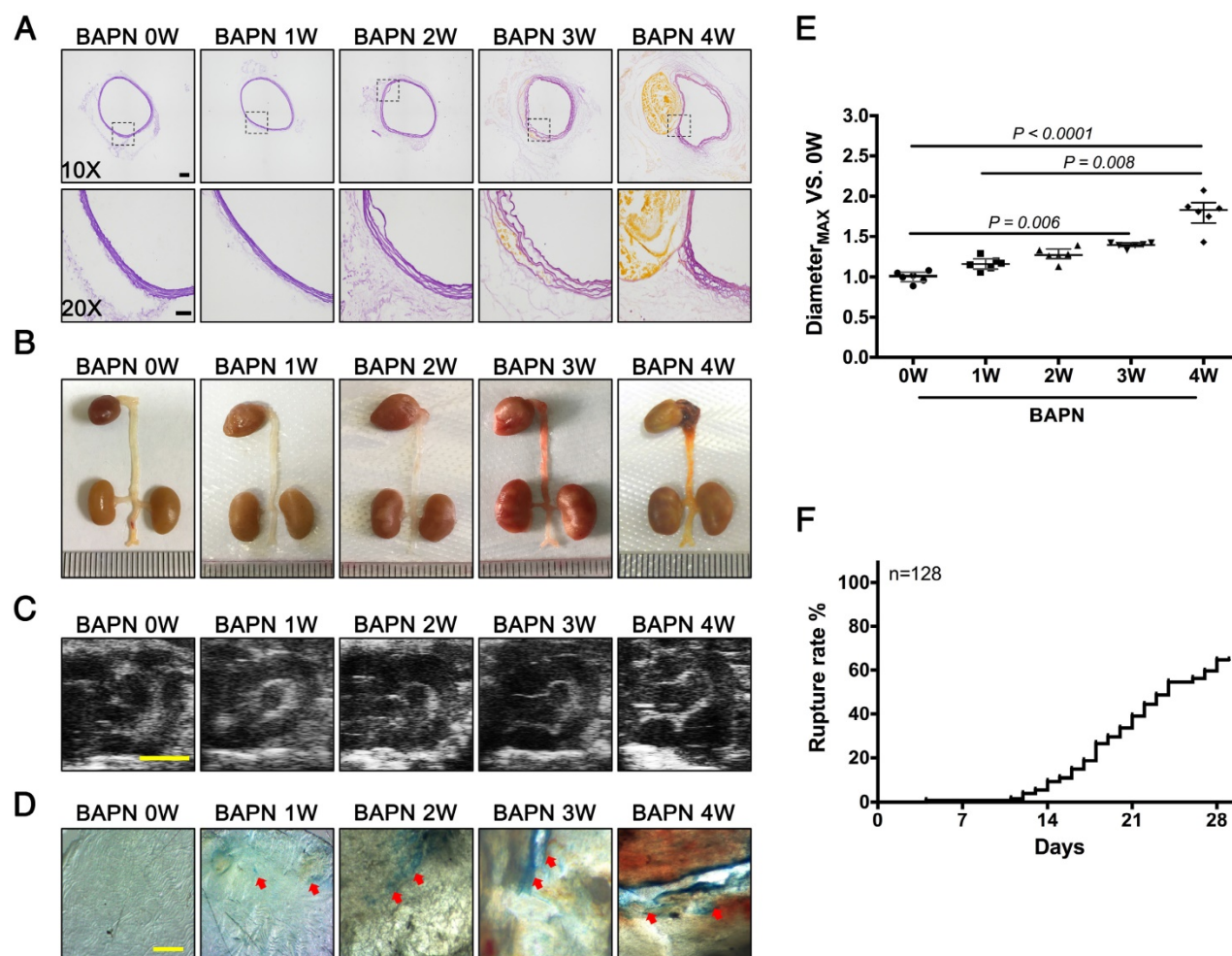


Figure 1. Pathological features of TAD in different stages. Mice were fed BAPN for 0, 1, 2, 3, and 4 weeks, respectively, to simulate the different stages of TAD development. **(A)** Staining of elastin in the aortic arch in mice. High-power view (20X) of the rectangular areas is shown in the lower rows in each panel (10X). Scale bars on the upper and lower panels, 100 μ m and 50 μ m, respectively. **(B)** Representative photographs of macroscopic features of TAD in different groups. **(C)** Ultrasound of the aortic arch from different groups (scale bar, 2 mm). **(D)** Evans blue staining of the aortic arch from different groups. Arrow indicates endothelial injury (scale bar, 5 mm). **(E)** Vessel diameters in mice from different groups. Data are presented as median \pm interquartile range (IQR), $n = 6$ for each time point. The probability value was calculated with K-W test. **(F)** Rupture rates in mice in progressive TAD models, $n = 128$. The normality of each group was validated with Kolmogorov-Smirnov test (K-S test).

Characterization of a MRI probe targeting Col-IV

We synthesized the polypeptide (Cys-Gly-Gly-Gly-Lys-Pro-Leu-Val-Trp-Leu-Lys, KLWVLPK) to target Col-IV [25] and modified it with Rhodamine B (RhB, as an internal probe tacking control) and DOTA-Gd (MRI contrast agent) to form the multifunctional compound Col-IV-DOTA-Gd-RhB (CDR). The retention times of purified Col-IV-RhB (CR) and CDR determined by HPLC were 5.50 min and 3.53 min, respectively (Fig. 3A). The increased polarity of CDR would decrease the retention time in reverse phase-HPLC compared with CR, so the change in appearance time demonstrated the success of the reaction. CDR was characterized separately for its fluorescence and MRI properties. Ultraviolet spectrophotometry showed absorption of CDR in the

band from 500 nm to 600 nm, with maximum absorption at 564 nm reflecting RhB, indicating successful synthesis (Fig. 3B). The fluorescence data in water (Fig. 3C) and cells (Fig. 3D) revealed corresponding fluorescence intensities under different concentrations of CDR. The fluorescence intensity of CDR increased in a concentration-dependent manner (Fig. 3C), indicating that CDR is suitable for different fluorescence requirements. Simultaneously, CDR also exhibited a linearly dose-dependent fluorescence intensity in vascular smooth muscle cells (VSMCs), demonstrating its suitability for fluorescence imaging *in vivo*. MRI detection in water (Fig. 3E, F) and cells (Fig. 3G, H) showed that the R1 value increased linearly with increasing concentrations of Gd³⁺ ($r^2 = 0.9920$, $p < 0.0001$ in water; $r^2 = 0.9930$, $p < 0.0001$ in cells). These results demonstrated the suitability of CDR for both fluorescence and MR imaging.

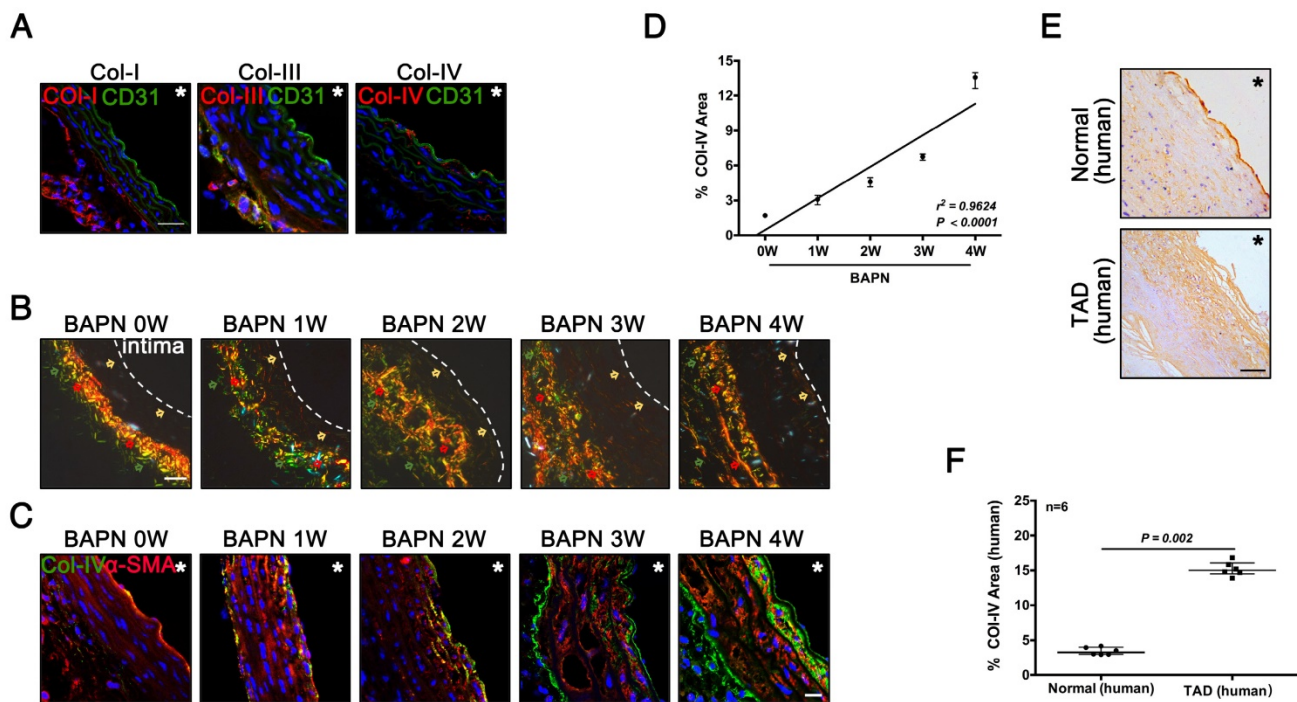


Figure 2. Collagen exposure after endothelial injury as an early signal of TAD development. (A) Frozen sections of the aortic arch in control mice were stained for Col-I/III/IV (scale bar, 25 μ m). (B) Sirius Red staining of the aortic arch at different time points (red arrow, Col-I; green arrow, Col-III; faint yellow arrow, Col-IV; white dashed line, intima; scale bar, 25 μ m). (C) Frozen sections of the aortic arch from different groups, stained for Col-IV (scale bar, 10 μ m). (D) Correlation between percentage Col-IV-positive area in the aortic arch and stage of TAD development ($r^2 = 0.9624$, $p < 0.0001$, $n = 10$ for each time point). The correlation coefficient and probability value were calculated with Spearman's correlation test. (E) Immunohistochemistry for Col-IV in normal and TAD human tissues (scale bar, 25 μ m). (F) Percentage Col-IV-positive area in D (median \pm IQR, $n = 6$, $p = 0.002$). The probability value was calculated with Mann-Whitney U test. * indicate the vascular lumen. The normality of each group was validated with Kolmogorov-Smirnov test (K-S test).

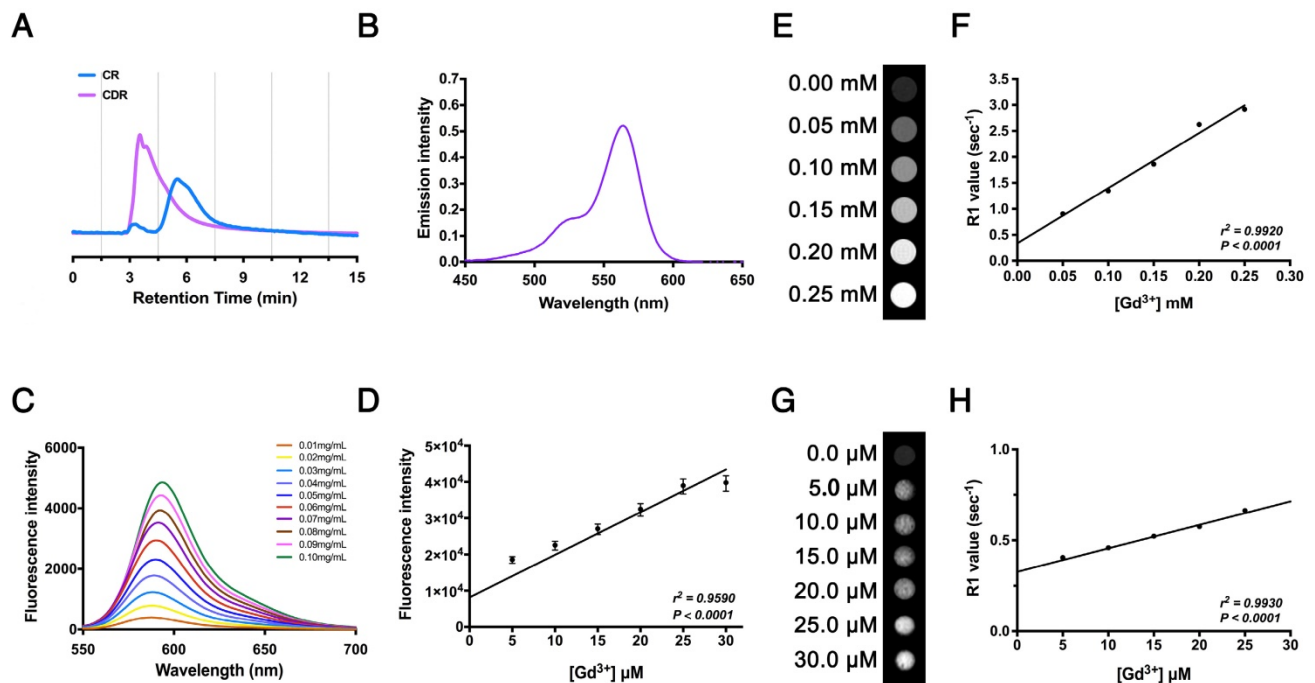


Figure 3. Characterization of Col-IV-DOTA-Gd-RhB molecular probes. (A) HPLC for Col-IV and CDR. (B) Ultraviolet absorption spectrum for CDR. (C) Fluorescence curve for CDR at different concentrations. (D) Fluorescence intensities of CDR in SMCs at different concentrations ($r^2 = 0.9590$, $p < 0.0001$, $n = 4$). The correlation coefficient and probability value were calculated with Spearman's correlation test. (E) Unbound relaxivity of CDR at 7 T. The relaxivity of unbound CDR at 7 T was obtained by measuring T1 at concentrations of 0–0.25 mM in PBS. (F) R1 value measured by MRI was linearly correlated with Gd^{3+} content ($r^2 = 0.9920$, $p < 0.0001$). The correlation coefficient and probability value were calculated with Pearson's correlation test. (G) Bound relaxivity of CDR at 7 T. The relaxivity of bound CDR in SMCs at 7 T was measured by incubating SMCs with CDR at 0–0.30 μ M. (H) R1 value measured by MRI was linearly correlated with Gd^{3+} content ($r^2 = 0.9930$, $p < 0.0001$). The correlation coefficient and probability value were calculated with Pearson's correlation test. The normality of each group was validated with Kolmogorov-Smirnov test (K-S test).

VSMCs, ECs, and macrophages are major cell types involved in the pathological process of TAD. To evaluate the specificity of Col-IV-DOTA-RhB (CDR), vascular smooth muscle cells (VSMCs), endothelial cells (ECs), and macrophages were incubated with CDR. Immunofluorescence staining showed that Col-IV is expressed in VSMCs (among three cells), and Col-IV-bound RhB signal was only seen in VSMCs, which is consistent with the fact that VSMCs express and secrete collagens including Col-IV as

extracellular matrix (Fig. 4A). Fluorescence quantification confirmed that there were significantly more RhB-positive VSMC cells compared with ECs or macrophages at different Gd^{3+} concentrations, and that the fluorescence in VSMCs positively increased with concentrations of CDR ($r^2 = 0.9643$, $p < 0.0001$; Fig. 4B). Hoechst dye staining and flow cytometry analysis showed that CDR has very low toxicity (Fig. 4C).

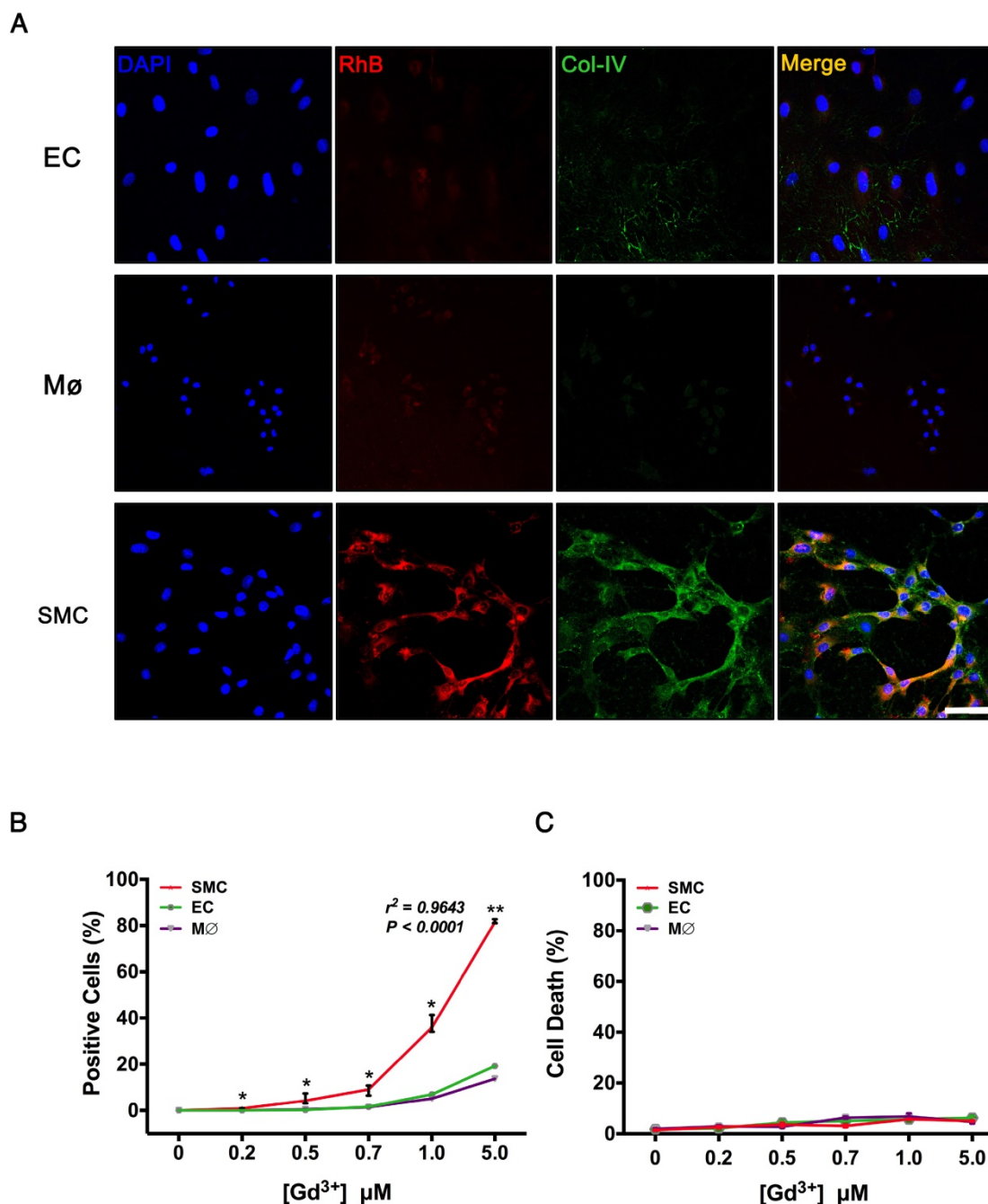


Figure 4. Target specificity of CDR in vitro. (A) Immunofluorescence staining in VSMCs, macrophages, and ECs after incubation with CDR for 24 h (red, CDR; green, Col-IV, scale bar, 25 μ m). **(B)** Percentage of positive cells (CDR⁺) in the three groups after incubation with CDR for 24 h. The probability value of each point was calculated with K-W test. The correlation coefficient was calculated with Spearman's correlation test ($r^2 = 0.9643$, $p < 0.0001$; median \pm IQR, $n = 4$). **(C)** Cytotoxicity (Hoechst- cells / Total cells) calculated by flow cytometry after incubation with CDR for 24 h (median \pm IQR, $n = 4$). The probability value of each point was calculated with K-W test. The normality of each group was validated with Kolmogorov-Smirnov test (K-S test).

To test if CDR can bind to the Col-IV secreted on the VSMC membrane surface and cannot be taken up by VSMCs, we performed the following experiments. The VSMCs were incubated with CDRs at high Gd^{3+} concentrations (5.0 μM). After 4 h, the cells were washed with phosphate-buffered saline (PBS) and imaged by confocal laser scanning microscopy. A cover slip with VSMCs was fixed by 4% paraformaldehyde to penetrate the cell membrane; another group of cells on the cover slip were not fixed to maintain cell integrity. DAPI staining was used to indicate cell viability. The results show that RhB signal appeared on the membrane surface of living VSMCs, and appeared in the cytoplasm when VSMCs were fixed (Fig. S1). Thus, our data reveal that CDR bind to Col-IV secreted as extracellular matrix by VSMCs.

Preclinical value of molecular MRI for early detection of TAD

We next evaluated the efficacy of CDR for detecting TAD by MRI, bioluminescence imaging (BLI), and histopathology. Mice were tail vein-injected with CDR or commercial DOTA-Gd (CG) after administration of BAPN for 0, 2, 3, and 4 weeks, followed by MRI, BLI, and histopathological examination (Fig. 5A). The thoracic aorta perpendicular to the vessel axis was visualized by MRI at different stages of TAD (Fig. 5B). MRI was carried out after injection of CDR or CG after 0, 2 or 4 weeks of BAPN administration. We initially compared the sensitivities of CDR and CG for the detection of early TAD. No signal was detected in the thoracic aorta in mice after injection of CDR and CG before BAPN administration. However, signal enhancement was detected in mice injected with CDR after 2 weeks of BAPN treatment, while the MRI signal after injection of CDR following 4 weeks of BAPN was still higher than the signal after injection of CG. BLI indicated a significant fluorescence signal enhancement in the thoracic aorta after 2 weeks of BAPN administration, which increased with progression of TAD (Fig. 5C). In addition, BLI analysis of the thoracic aorta showed that the fluorescence signal increased significantly with the development of TAD. BLI analysis of the kidney (enriched with Col-IV) showed that the accumulation of CDR in the kidney gradually reduced with progressive development of TAD. These results indicated that CDR was enriched at the dissection (Fig. 5D). As Figure 2 showed that both EC loss and Col-IV expression gradually increased with the progression of TAD, we assessed the efficacy of CDR for detecting dissection. Signal enhancement was observed in the dissection area, which increased with

the development of dissection. Immunofluorescence staining showed RhB fluorescence at the position of the intima tear (Fig. 5E). Similarly, we also tested the CDR signal in the abdominal aorta at different times of BAPN administration: we detected no CDR signal and dissection of the abdominal aorta at different stages of TAAD (Fig. S2). The normalized signal enhancement (%NSE) analyzed by MRI increased with TAD development (Fig. 5F). The percentage area of RhB-positivity in frozen sections increased with TAD formation, consistent with the trend in MRI analysis (Fig. 5G). These results suggested that CDR could provide significant contrast enhancement to aid the detection of TAD as early as 2 weeks, by targeting exposed Col-IV on the injured intima.

Predictive value of molecular MRI for assessing risk of TAD rupture

As noted above, early stage TAD could be detected by MRI following injection of CDR (Fig. 5). We next determined if CDR could also predict rupture of the TAD. We performed MRI examinations of CDR-injected mice after 2 weeks of BAPN administration, and subsequently monitored them for survival. %NSE and pathology were examined upon death or sacrifice after 4 weeks of BAPN administration (Fig. 6A). The MRI signal was enhanced at the location of the dissection, and increased with the severity of the dissection (Fig. 6B). Mice were grouped according the median %NSE, and the survival rate was significantly lower in mice with %NSE > median (defined as ruptured TAD group), compared with those with %NSE < median group (defined as stable thoracic aortic dissection, stable TAD groups) (Fig. 6C). The %NSE in the rupture TAD group was significantly higher than that in the stable TAD group (Fig. 6D). We confirmed the relationship between MRI signal and TAD rupture by correlation analysis of %NSE and rupture time after BAPN administration, and showed that %NSE was significantly negatively correlated with rupture time in the total model mouse ($r^2 = 0.8482$, $p = 0.001$) (Fig. 6E) and in the death group ($r^2 = 0.8281$, $p = 0.032$) (Fig. 6F). This suggested that MRI based on the CDR probe is able to predict the occurrence of TAD rupture.

Discussion

In the present study, we demonstrated the ability of MRI using a Col-IV-targeted molecular probe to detect early TAD and assess the risk of TAD rupture. During TAD development, EC loss in the descending aorta occurred at an early stage of TAD (after 1 week of BAPN administration), while obvious elastic-fiber disorder and vascular dilatation did not appear at the same stage (not until after 3 weeks). Col-IV was

predominantly expressed beneath the EC sheet in normal vascular. In BAPN-induced TAD models, Col-IV content gradually increased with BAPN administration and Col-IV deposition occurred in the adventitia after 3 weeks of BAPN administration, due to the compensatory repair of degenerated aorta. Importantly, CDR identifies the exposed Col-IV at the site of injured intima in the early stage of aortic dissection. Administration of CDR is by intravenous injected; therefore, the CDR enters the circulation with little access to the adventitia side. Thus, CDR-positive signals indicate endothelial injury, which predicts the formation of dissection.

Our results suggested that molecular MRI with intravenous administration of CDR could provide visual information of early Col-IV exposure, as an early target of TAD. This conclusion was supported by the co-localization of Col-IV *in vivo* determined by MRI, BLI, and histopathology. We showed that administration of CDR resulted in a significantly enhanced MRI signal after 2 weeks of BAPN administration, while no such signal enhancement was observed following CR administration at the same time point. The BLI results were consistent with the MRI results. The specificity of CDR was demonstrated *in vivo* during the different stages of TAD. Histological staining confirmed the accumulation of CDR in areas with disordered elastic fibers, and obvious RhB fluorescence was detected in the position of the intima tear. In contrast, no fluorescence signal was observed following CDR injection in healthy animals and abdominal aorta where no dissection took place during the different stages of TAD. The pathological results were consistent with those of MRI and BLI, and all suggested that molecular MRI with CDR could detect early TAD.

Our present study also established a correlation between early intimal injury and the severity of TAD. We showed an association between an increase in %NSE and an increase in ruptured dissection. Moreover, the time to TAD rupture increased gradually with increasing signal. There was a significant positive correlation between %NSE and rupture time. Overall, these results suggest that CDR can identify the severity of dissection and predict the risk of TAD rupture.

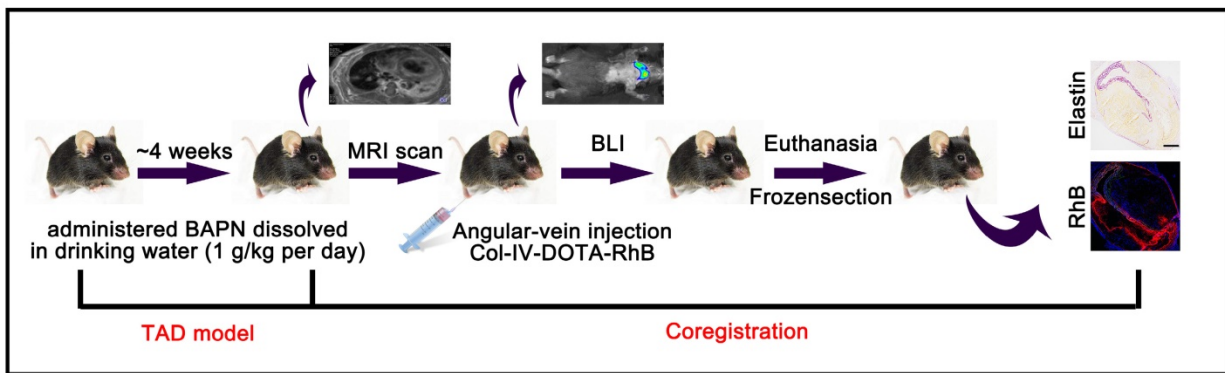
Notably, other biological targets involved in abdominal aortic aneurysms (AAAs) pathology have been investigated previously, such as inflammation, VSMCs apoptosis, and ECM degradation [31]. Macrophages aggravate AAAs by releasing proteolytic enzymes such as matrix

metalloproteinases (MMPs), resulting in significant remodeling and degradation of the ECM [32]. Previous studies utilized super paramagnetic iron oxide to detect AAAs by monitoring macrophage activities in experimental AAA model and AAA patients. In animal studies, they used SPIO-enhanced imaging to localize active inflammation and intraluminal thrombus. In associated human studies, USPIO-enhanced MRI has also been reported to enable successful visualization of severe inflammation within AAAs. The authors reported that patients with significant mural uptake of USPIO had a threefold higher AAAs growth rate (measured over 6 months) compared to those with no or non-specific USPIO uptake [33]. Degradation of elastic fibers was related to the development of the aneurysm. The authors used an elastin-specific magnetic resonance imaging contrast agent to monitor the AAAs by assessing the elastin content within the ascending aortic aneurysm wall. MRI based on targeted probes was able to detect advanced, but not early, aneurysms [34]. An imbalance in collagen deposition/degradation, especially Col-I, is a key factor in the prognosis of AAAs [35]. A Col-I targeted contrast agent (CNA-35) was constructed to detect collagen in the adventitia by MRI, and suggested that the levels of Col-I in early-stage AAAs are associated with severity [36]. However, MRI using a Col-I-targeted probe did not predict the risk of dissection rupture. The current study thus has two strengths compared with previous studies. First, for the first time it achieved non-invasive early diagnosis of TAD in preclinical animal studies by MRI and BLI. Second, it suggested the early prediction of TAD rupture risk.

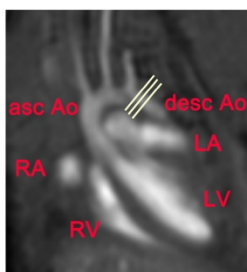
Our present study has several limitations. One limitation is the lack of examination of reliable MR image co-registration or correlation with histological sections in dissection patients, which requires excision of the entire dissection and is not routinely performed in clinical practice. Another limitation is although we showed that CDR can be used to detect early TAD in a mouse model, this agent needs to be investigated further in large animals and eventually confirmed in humans.

In conclusion, this study demonstrated the abilities of MRI and fluorescence imaging with molecular CDR to detect early TAD and to predict rupture of TAD. Early diagnosis and risk prediction of dissections play an important role in their clinical management. The current study thus proposes a potential method for dissection screening in high-risk patient populations, and for monitoring disease progression and therapeutic response.

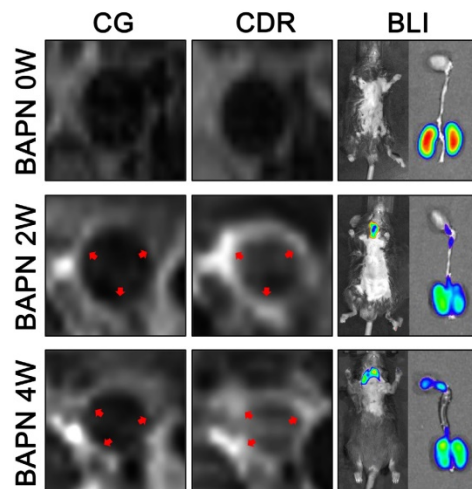
A



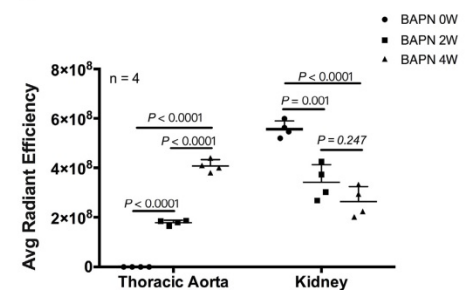
B



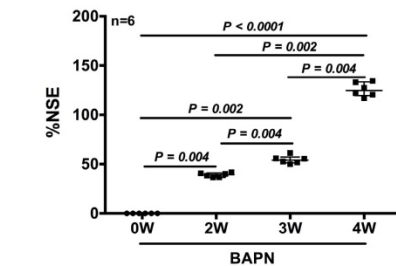
C



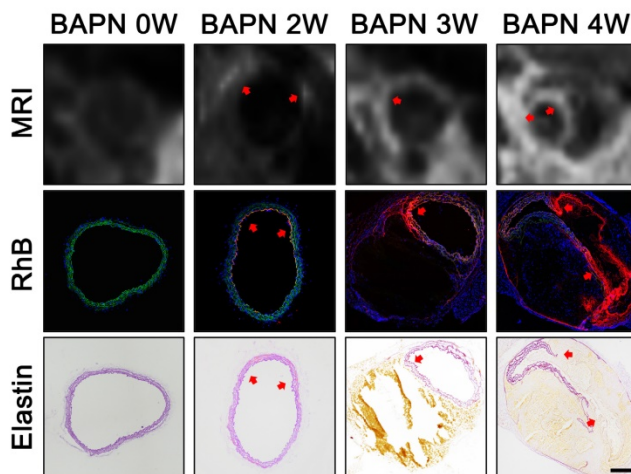
D



E



F



G

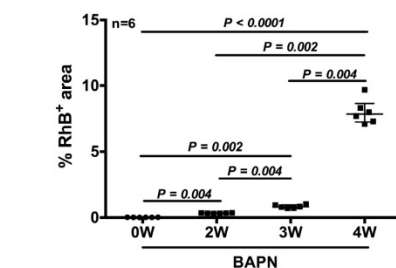


Figure 5. MRI and BLI of TAD in mice. (A) MRI, BLI and Pathological imaging of TAD in mice administered BAPN. (B) Line indicates cross-sectional MRI slice of descending aorta where T1 signal enhancement was acquired. (C) Representative MRI images of mice 6 h after injection with CG and CDR, following BAPN administration for 0, 2, and 4 weeks. Mice were examined by BL after MR imaging. The red arrows for the CG or CDR groups indicate the same position. (D) Quantification of fluorescence efficiency in thoracic aorta and kidney after CDR injection at different stages of TAD (mean \pm SD, $n = 4$). The probability value of each group was calculated with one way ANOVA and adjusted with the post hoc test. (E) MRI (upper), fluorescence (middle) and histology (bottom) images of the aortas from WT mice treated with BAPN for different times (arrow indicates tear or elastin disorder; scale bar, 100 μ m). (F) R1 value of descending aorta wall in mice administered BAPN for different times (median \pm IQR, $n = 6$). The probability value of each group was calculated with Mann-Whitney U test and adjusted with the Bonferroni correction. (G) Quantification of percentage RhB-positive area at different times (median \pm IQR, $n = 6$). The probability value of each group was calculated with Mann-Whitney U test and adjusted with the Bonferroni correction. The normality of each group was validated with Kolmogorov-Smirnov test (K-S test).

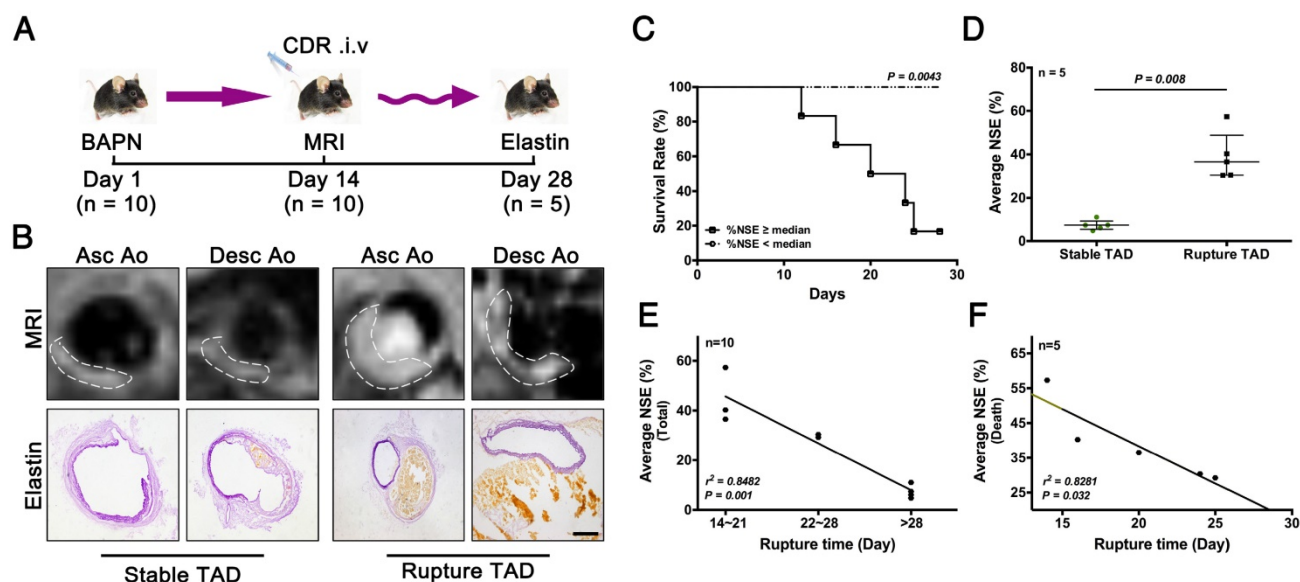


Figure 6. Correlation between %NSE calculated by CDR-enhanced MRI and severity of TAD. (A) CDR-enhanced MRI after 2 weeks of BAPN administration, and severity of dissection detected by elastin staining after 4 weeks of BAPN administration. (B) MRI (upper) and corresponding elastin-staining (bottom) images of ascending aorta and descending aorta, respectively, at different stages of TAD development (white dashed line indicates ROIs). MRI was performed after 2 weeks of BAPN administration and elastin staining was performed after death or 4 weeks of BAPN administration in mice. (C) Survival curves for two groups (%NSE \geq median and %NSE $<$ median) ($p = 0.0043$, $n = 10$). (D) Quantitative analysis of %NSE in both groups (median \pm IQR, $p = 0.008$, $n = 5$). The probability value of each point was calculated with Mann-Whitney U test. (E) Correlation between %NSE and rupture time in all mice ($r^2 = 0.8482$, $p = 0.001$, $n = 10$). The correlation coefficient was calculated with Spearman's correlation test. (F) Correlation between %NSE and rupture time in the death group ($r^2 = 0.8281$, $p = 0.032$, $n = 5$). The correlation coefficient was calculated with Pearson's correlation test. The normality of each group was validated with Kolmogorov-Smirnov test (K-S test).

Abbreviations

Col-IV: type IV collagen; Col-I: type I collagen; Col-III: type III collagen; CDR: Col-IV-DOTA-Gd-rhodamine B; MRI: magnetic resonance imaging; NSE: normalized signal enhancement; TAD: thoracic aortic dissection; CTA: computed tomography angiography; TTE: transthoracic echocardiography; EC: endothelial cell; BAPN: 3-aminopropionitrile fumarate salt; RhB: rhodamine B; HPLC: high performance liquid chromatography; SMC: smooth muscle cell; VSMC: vascular smooth muscle cell; FBS: fetal bovine serum; PBS: phosphate buffer saline; ROI: region of interest; SNR: signal to noise ratio; CNR: contrast to noise ratio; SD: standard deviation; IQR: interquartile range; CR: Col-IV-RhB; BLI: bioluminescence imaging; CG: commercial DOTA-Gd; AAA: abdominal aortic aneurysm; MMP: matrix metalloproteinase.

Supplementary Material

Supplementary figures.

<http://www.thno.org/v08p0437s1.pdf>

Acknowledgement

This study was supported by grants from the National Key R & D Program of China

(2016YFC0903000), the National Science Foundation of China (91339000 and 91539121), Program for Innovative Research Team (IRT_17R76).

Competing Interests

The authors have declared that no competing interest exists.

References

- Khan S, Verma V, Verma S, Polzer S, Jha S. Assessing the potential risk of rupture of abdominal aortic aneurysms. *Clin Radiol.* 2015; 70: 11-20.
- Katzen BT, Dake MD, MacLean AA, Wang DS. Endovascular repair of abdominal and thoracic aortic aneurysms. *Circulation.* 2005; 112: 1663-75.
- Goldfinger JZ, Halperin JL, Marin ML, Stewart AS, Eagle KA, Fuster V. Thoracic aortic aneurysm and dissection. *J Am Coll Cardiol.* 2014; 64: 1725-39.
- Erbel R, Aboyans V, Boileau C, Bossone E, Bartolomeo RD, Eggebrecht H, et al. 2014 ESC Guidelines on the diagnosis and treatment of aortic diseases: Document covering acute and chronic aortic diseases of the thoracic and abdominal aorta of the adult. The Task Force for the Diagnosis and Treatment of Aortic Diseases of the European Society of Cardiology (ESC). *Eur Heart J.* 2014; 35: 2873-926.
- Wu D, Shen YH, Russell L, Coselli JS, LeMaire SA. Molecular mechanisms of thoracic aortic dissection. *J Surg Res.* 2013; 184: 907-24.
- Lindsay ME, Dietz HC. Lessons on the pathogenesis of aneurysm from heritable conditions. *Nature.* 2011; 473: 308-16.
- Evangalista A, Carro A, Moral S, Teixido-Tura G, Rodriguez-Palmares JF, Cuellar H, et al. Imaging modalities for the early diagnosis of acute aortic syndrome. *Nature reviews Cardiology.* 2013; 10: 477-86.
- McBride OM, Joshi NV, Robson JM, MacGillivray TJ, Gray CD, Fletcher AM, et al. Positron Emission Tomography and Magnetic Resonance Imaging of Cellular Inflammation in Patients with Abdominal Aortic Aneurysms. *Eur J Vasc Endovasc Surg.* 2016; 51: 518-26.
- Worthley SG, Helft G, Fayad ZA, Fuster V, Zaman AG, Shinnar M, et al. Images in cardiovascular medicine. Magnetic resonance imaging and asymptomatic aortic dissection. *Circulation.* 2000; 101: 2771.
- Nyborg AC, Moll JR, Wegrzyn RD, Havas D, Hutter-Paier B, Feuerstein GG, et al. In vivo and ex vivo imaging of amyloid-beta cascade aggregates with a Pronucleon peptide. *Journal of Alzheimer's disease : JAD.* 2013; 34: 957-67.

11. Viola KL, Sbarboro J, Sureka R, De M, Bicca MA, Wang J, et al. Towards non-invasive diagnostic imaging of early-stage Alzheimer's disease. *Nature nanotechnology*. 2015; 10: 91-8.
12. Malik G, Knowles LM, Dhir R, Xu S, Yang S, Ruoslahti E, et al. Plasma fibronectin promotes lung metastasis by contributions to fibrin clots and tumor cell invasion. *Cancer research*. 2010; 70: 4327-34.
13. Zhou Z, Qutaish M, Han Z, Schur RM, Liu Y, Wilson DL, et al. MRI detection of breast cancer micrometastases with a fibronectin-targeting contrast agent. *Nat Commun*. 2015; 6: 7984.
14. Kuivaniemi H, Ryer EJ, Elmore JR, Tromp G. Understanding the pathogenesis of abdominal aortic aneurysms. Expert review of cardiovascular therapy. 2015; 13: 975-87.
15. Baxter BT, Terrin MC, Dalman RL. Medical management of small abdominal aortic aneurysms. *Circulation*. 2008; 117: 1883-9.
16. Nienaber CA, Clough RE. Management of acute aortic dissection. *Lancet*. 2015; 385: 800-11.
17. El-Hamamsy I, Yacoub MH. Cellular and molecular mechanisms of thoracic aortic aneurysms. *Nat Rev Cardiol*. 2009; 6: 771-86.
18. Kalluri R. Basement membranes: structure, assembly and role in tumour angiogenesis. *Nat Rev Cancer*. 2003; 3: 422-33.
19. Cherifi H, Gogly B, Loison-Robert LS, Couty L, Ferre FC, Nassif A, et al. Comparative study of abdominal and thoracic aortic aneurysms: their pathogenesis and a gingival fibroblasts-based ex vivo treatment. *Springerplus*. 2015; 4: 231.
20. Chan JM, Zhang L, Tong R, Ghosh D, Gao W, Liao G, et al. Spatiotemporal controlled delivery of nanoparticles to injured vasculature. *Proc Natl Acad Sci U S A*. 2010; 107: 2213-8.
21. Fredman G, Kamaly N, Spolitu S, Milton J, Ghorpade D, Chiasson R, et al. Targeted nanoparticles containing the proresolving peptide Ac2-26 protect against advanced atherosclerosis in hypercholesterolemic mice. *Sci Transl Med*. 2015; 7: 275ra20.
22. Yu M, Amengual J, Menon A, Kamaly N, Zhou F, Xu X, et al. Targeted Nanotherapeutics Encapsulating Liver X Receptor Agonist GW3965 Enhance Antiatherogenic Effects without Adverse Effects on Hepatic Lipid Metabolism in Ldlr^{-/-} Mice. *Adv Healthc Mater*. 2017.
23. Kurihara T, Shimizu-Hirota R, Shimoda M, Adachi T, Shimizu H, Weiss SJ, et al. Neutrophil-derived matrix metalloproteinase 9 triggers acute aortic dissection. *Circulation*. 2012; 126: 3070-80.
24. Ren W, Liu Y, Wang X, Jia L, Piao C, Lan F, et al. beta-Aminopropionitrile monofumarate induces thoracic aortic dissection in C57BL/6 mice. *Sci Rep*. 2016; 6: 28149.
25. Kamaly N, Fredman G, Subramanian M, Gadde S, Pesic A, Cheung L, et al. Development and in vivo efficacy of targeted polymeric inflammation-resolving nanoparticles. *Proc Natl Acad Sci U S A*. 2013; 110: 6506-11.
26. Zheng S, Li W, Xu M, Bai X, Zhou Z, Han J, et al. Calcitonin gene-related peptide promotes angiogenesis via AMP-activated protein kinase. *American journal of physiology Cell physiology*. 2010; 299: C1485-92.
27. Xu Q, Saxena A, Björkbacka H, Ström Å, Rattik S, Berg KE, et al. Mobilization of Regulatory T Cells in Response to Carotid Injury Does Not Influence Subsequent Neointima Formation. *PLoS ONE*. 2012; 7: e51556.
28. Wang Y, Ait-Oufella H, Herbin O, Bonnin P, Ramkhalawon B, Taleb S, et al. TGF-beta activity protects against inflammatory aortic aneurysm progression and complications in angiotensin II-infused mice. *The Journal of clinical investigation*. 2010; 120: 422-32.
29. Zhang C, van der Voort D, Shi H, Zhang R, Qing Y, Hiraoka S, et al. Matricellular protein CCN3 mitigates abdominal aortic aneurysm. *The Journal of clinical investigation*. 2016; 126: 2012.
30. Zhang JM, Wang Y, Miao YJ, Zhang Y, Wu YN, Jia LX, et al. Knockout of CD8 delays reendothelialization and accelerates neointima formation in injured arteries of mouse via TNF-alpha inhibiting the endothelial cells migration. *PLoS One*. 2013; 8: e62001.
31. Sadat U, Taviani V, Patterson AJ, Young VE, Graves MJ, Teng Z, et al. Ultrasmall superparamagnetic iron oxide-enhanced magnetic resonance imaging of abdominal aortic aneurysms—a feasibility study. *Eur J Vasc Endovasc Surg*. 2011; 41: 167-74.
32. Gandhi RH, Irizarry E, Cantor JO, Keller S, Nackman GB, Halpern VJ, et al. Analysis of elastin cross-linking and the connective tissue matrix of abdominal aortic aneurysms. *Surgery*. 1994; 115: 617-20.
33. Emeto TI, Alele FO, Smith AM, Smith FM, Dougan T, Golledge J. Use of Nanoparticles As Contrast Agents for the Functional and Molecular Imaging of Abdominal Aortic Aneurysm. *Front Cardiovasc Med*. 2017; 4: 16.
34. Okamura H, Pisani LJ, Dalal AR, Emrich F, Dake BA, Arakawa M, et al. Assessment of elastin deficit in a Marfan mouse aneurysm model using an elastin-specific magnetic resonance imaging contrast agent. *Circ Cardiovasc Imaging*. 2014; 7: 690-6.
35. Abdul-Hussien H, Soekhoe RGV, Weber E, von der Thüsen JH, Kleemann R, Mulder A, et al. Collagen Degradation in the Abdominal Aneurysm. *The American Journal of Pathology*. 2007; 170: 809-17.
36. Klink A, Heynens J, Herranz B, Lobatto ME, Arias T, Sanders HM, et al. In vivo characterization of a new abdominal aortic aneurysm mouse model with conventional and molecular magnetic resonance imaging. *J Am Coll Cardiol*. 2011; 58: 2522-30.